Resultant Radius of Curvature of Stylet-and-Tube Steerable Needles Based on the Mechanical Properties of the Soft Tissue, and the Needle

Fan Yang[1], Mahdieh Babaiasl[2], Yao Chen[3], Jow-Lian Ding[4], John P. Swensen[5]

***Abstract*— Steerable needles have been widely researched in recent years, and they have multiple potential roles in the medical area. The flexibility and capability of avoiding obstacles allow the steerable needles to be applied in the biopsy, drug delivery and other medical applications that require a high degree of freedom and control accuracy. Radius of Curvature (ROC) of the needle while inserting in the soft tissue is an important parameter for evaluation of the efficacy, and steerability of these flexible needles. For our Fracture-directed Stylet-and-Tube Steerable Needles, it is important to find a relationship among the resultant insertion ROC, pre-set wire shape and the Young's Modulus of soft tissue to characterize this class of steerable needles. In this paper, an approach is provided for obtaining resultant ROC using stylet and tissue's mechanical properties. A finite element analysis is also conducted to support the reliability of the model. This work sets the foundation for other researchers to predict the insertion ROC based on the mechanical properties of the needle, and the soft tissue that is being inserted.**

***Index Terms*— Steerable Needles, Medical Robots, SEBS Tissue, Bending Stiffness, Curvature**

I. Introduction

Different factors affect the radius of curvature of steerable needles while being inserted into the soft tissue. These factors include the mechanical properties of the soft tissue, tip geometry, and mechanical properties of the needle [1], [2], [3]. Several research groups have developed mechanics-based as well as non-physics based models to predict the insertion radius of traditional steerable needles based on the properties of the needle, and soft tissue [4], [5], [6]. An analysis of interaction forces between the needle and soft tissue was developed by Misra et al.[4] for bevel-tip steerable needles. A finite element analysis was conducted to evaluate the forces on the needle tip. A method to calculate the stored kinetic energy and the relationship between multiple tubes' curvatures and their bending stiffnesses for concentric tube robots have been developed by Rucker et al. [7].

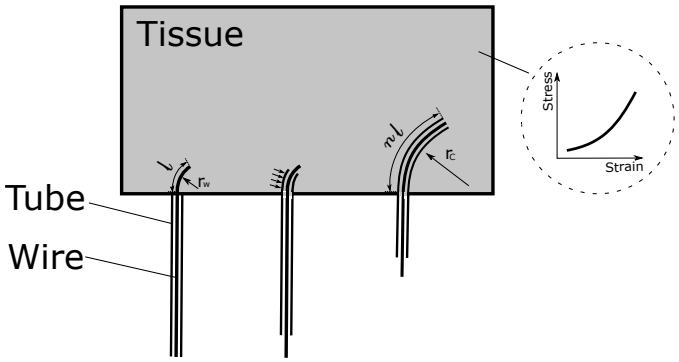

Fig. 1. Stylet-and-Tube Steerable Needles, in which the direction of the tissue fracture is controlled with the inner wire, and then the outer tube follows [1]. The combined radius of curvature is depend on step length, preset radius of the wire, tissue's mechanical properties, and tube & wire mechanical properties.

We have proposed a new class of steerable needles that we call fracture-directed stylet-and-tube steerable needles in which the direction of the tissue fracture is controlled by an inner stylet and then the flexible outer tube follows. This method has shown to achieve a radius of curvature as low as 6 mm in soft tissue phantoms which is unachievable by traditional steerable needles [1]. In order to fully characterize these steerable needles, we need to find a model that can predict the ROC of the steerable needle inside the soft tissue based on the mechanical properties of the needle, and the soft medium. Our proposed fracture-directed stylet-and-tube steerable needles have similarities to concentric tube robots. Thereby, we attempt to fit the wire-tube-tissue channel model into the concentric tube model to simplify the mechanical analysis of the insertion and find out the relationship between insertion ROC and the parameters of selected pre-curved wire. In other words, we propose to suppose the tissue channel as an outer tube and treat the needle and the tissue channel as concentric tubes.

In this paper, ROC of the stylet-and-tube steerable needle while insertion into soft tissue is predicted which is a function of bending stiffnesses of the tube, stylet, and soft tissue as well as the step length. Fig. 1 shows the different parameters that affect the insertion radius of stylet-and-tube steerable needles. Note that ROC is also dependent on the step length of the inner stylet that is followed by the outer tube; however, in this paper, step length is considered to be constant and the

[1]Fan Yang is a Graduate Research Assistant with the School of Mechanical and Materials Engineering, Washington State University, Pullman, Washington, USA. fan.yang6@wsu.edu

[2]Mahdieh Babaiasl is a Graduate Research Assistant with the School of Mechanical and Materials Engineering, Washington State University, Pullman, Washington, USA. mahdieh.babaiasl@wsu.edu

[3]Yao Chen is a Graduate Research Assistant with the School of Mechanical and Materials Engineering, Washington State University, Pullman, Washington, USA. yao.chen@wsu.edu

[5]Jow-Lian Ding is a Professor with the School of Mechanical and Materials Engineering, Washington State University, Pullman, Washington, USA. jowlian_ding@wsu.edu

[4]John P. Swensen is an Assistant Professor with the School of Mechanical and Materials Engineering, Washington State University, Pullman, Washington, USA. john.swensen@wsu.edu

Manuscript 1655 submitted to 2020 IEEE/RSJ International Conference on Intelligent Robots and Systems. Received March 1, 2020.

full model involving the step length will be presented in the future research.

The experiments presented in this paper are based on soft tissue phantoms with the Young's Moduli in the range from 112.89 KPa to 229.57 KPa. This range coincides with the Young's Moduli of human tendon and stays within one magnitude difference with the Young's modulus of human muscle. [8]. The tissue phantoms with lower polymer ratios can be used for mimicking softer tissues in the human body for the same type of experiments.

II. Materials and Methods

In this section, the materials and methods used in the experiments are described. In the experiments, there are three different stiffnesses of tissue simulants, and three combinations of Nitinol tubes and wires. The Young's Moduli of tissue simulants, Nitinol tubes, and Nitinol wires are chosen across a certain range. The Nitinol wires involved in the experiments are heat-treated to generate the pre-curved shape, and the curvature of all pre-curved wires are constant. Nitinol tubes are polished and remain straight.

A. Nitinol Tubes and Wires

Most of Nitinol wires and tubes used in the experiments are manufactured by Confluent Medical Technologies (Scottsdale, AZ, USA), except the smallest Nitinol tube, which has 0.33mm outer diameter and 0.26 inner diameter, which is produced by Goodfellow Corporation (Coraopolis, PA, USA).

B. Heat Treatment of Nitinol Stylet and Its Recoverable Strain

The stylets used in the experiments are made of superelastic shape memory alloy, Nickel Titanium. As such, before heat treatment, it is necessary to calculate the maximum recoverable strain when determining the minimum pre-curved radius of stylet curvature for experiments. To ensure the stylet can be fully straightened without any plastic deformation, we decided to use the common conservative superelastic Nitinol strain limit of $\varepsilon = 8\%$ [9]. The relationship between recoverable strain limit (ε), and needle tip pre-curvature (κ) is:

$$\kappa = \frac{2\varepsilon}{D(1+\varepsilon)} \tag{1}$$

Then the minimum radius of needle curvature, r, can easily be calculated by inverting κ:

$$r = 1/\kappa. \tag{2}$$

The characteristics of the needles (consisting of the tube, and wire) used in our experiments are described in Table I. For these needles, the minimum precurved radii of 0.19mm, 0.29mm, and 0.47mm diameter stylets without plastic deformation are 1.29mm, 1.97mm, and 3.17mm, respectively. Three different preset radii of Nickel-Titanium stylets are 30mm, 60mm, and 90mm.

To fabricate the 30mm, 60mm, and 90mm constant radii of curvature, straight Nitinol wires are pressed in a steel mold (refer to Fig. 2), heated to $500^{\circ}C$ for 30 minutes, then quenched in water. Generally, for the heat treatment of Nitinol stylets with different diameters and radii of curvatures, heat treatment time needs to be raised up if Nitinol pieces have smaller diameters or preset radii. In this paper, 30 minutes heat treatment time was chosen to assure that the 0.19mm stylet can hold 30 mm radius of curvature under room temperature. Fig. 2 shows the three different radii after heat treatment that are used during experimentation.

Fig. 2. Steel heat treatment mold for Nitinol wires with three different radii. The Nitinol wires are put in the grooves and then put in the oven at 500^{o} C for about 30 minutes and then quenched to get the constant pre-curvatures.

C. Tissue Simulants

The material we used to simulate the biological tissues in this paper is Poly (styrene-b-ethylene-co-butylene-b-styrene) triblock copolymer (SEBS), produced by Kraton Polymers LLC (G1650, Houston, TX, USA). Soft tissue simulants made of SEBS are environmentally stable substitutes for water-based hydrogels [1], [10], [11], [12]. The tissues made of SEBS in mineral oil are optically clear which makes the imaging of the inside of the tissues easier. The Young's Moduli of SEBS tissue simulants are calculated from the compression tests. The density of this material is $\rho_{SEBS} = 910\frac{kg}{m^3}$. Mineral oil is used as the solvent for this material. The mineral oil involved in the experiments is white mineral oil with density of $\rho_{oil} = 0.85\frac{g}{mL}$. SEBS material and white mineral oil are mixed by weight, in which the fractions of polymer used in the experiments are 15%, and 25%. The mixture is then put into the oven at $120^{o}C$ for 2 to 8 hours (the more SEBS the mixture contains, the more time will be needed for melting), and is mixed occasionally to produce a homogeneous solution without any visible undissolved powder. The solution is then put in the vacuum chamber to release any air bubbles trapped into the mixture. It is then poured into the molds of rectangular shape with dimensions of $100 \times 100 \times 30 mm$. Pre-curved Nitinol wires were placed in the mold before the solution was poured to create channel with constant curvatures

Manuscript 1655 submitted to 2020 IEEE/RSJ International Conference
on Intelligent Robots and Systems. Received March 1, 2020.

TABLE I
PARAMETERS OF THE TUBE, AND WIRE WITH DIFFERENT BENDING STIFFNESSES: LOW, MEDIUM, AND HIGH

	Low Bending Stiffness		Medium Bending Stiffness		High Bending Stiffness	
Parameters	**Tube**	**Wire**	**Tube**	**Wire**	**Tube**	**Wire**
Outer Diameter (mm)	0.33	0.19	0.57	0.29	0.85	0.47
Inner Diameter (mm)	0.26	-	0.32	-	0.52	-
Bending Stiffness (N/m)	2.68e-05	4.85e-06	3.55e-04	2.68e-05	1.65e-03	1.80e-04
Length (mm)	150	180	150	180	150	180
Young's Modulus (GPa)	75	75	75	75	75	75
Poisson's ratio	0.33	0.33	0.33	0.33	0.33	0.33

(Refer to Fig. 3). The tissue simulants are then let to cool down at room temperature before removing from the molds. Universal mold release was used in order to peel the tissue simulants off easily.

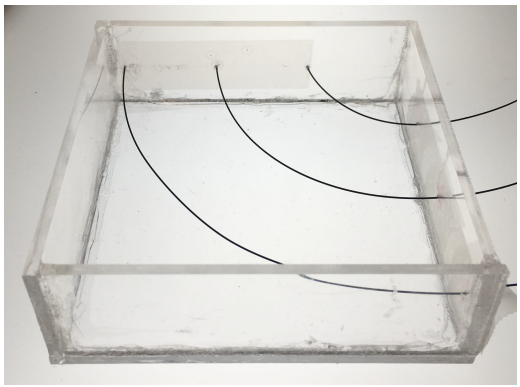

Fig. 3. Holes are drilled on walls of the acrylic container to setup Nitinol wires. These wires are used to create constant pre-cruvatures in soft tissue phantoms (The SEBS in mineral oil solution will be poured on them).

D. Compression Tests

In order to develop a suitable model for finding bending stiffnesses of tissues, Young's moduli of tissue phantoms need to be calculated first. Load versus displacement curves are obtained from compression tests. The static compression tests are performed with Instron 600DX machine controlled by Bluehill 3 software. Samples with the dimensions of 30mm diameter and 10mm thickness for each of the three types of SEBS tissue simulants (different stiffnesses) are manufactured. The strain rates of all the tests are fixed at $0.001\frac{1}{s}$ (needle insertion into the soft tissue is done at a low strain rate). The change of the gauge length is measured with a built-in sensor and the compressive load (F) was obtained from a 25 lb (approximately 111 N) S-type load cell connected to the machine. The data of displacement and Force was taken each 0.1(s). The strain of the samples is calculated by the following equation:

$$\varepsilon = \frac{\delta L}{L_0} \tag{3}$$

where L_0 is the initial thickness of the samples, and the stress of the tests can be calculated by the following equation:

$$\sigma = \frac{4F}{\pi D^2} \tag{4}$$

where D is the diameter of the samples.

Three tests are performed for each tissue stiffness. The average of the stress-strain data is calculated for each material using the three sets of data. The Young's Moduli of the tissue phantoms are calculated by finding the slope of the linear portion of the stress-strain curve.

E. Finite Element Analysis of the Resultant Curvature of the Needle, and Tissue Channel

Finite element analysis has been used for finding the behavior and consequent deflection in both active and passive steerable needle researches by Khashei Varnamkhasti et al.[13], Oldfield et al.[14] and Jushiddi et al.[15].

In fracture-directed stylet-and-tube needle steering approach, a channel is created first by an inner Nitinol stylet, and then is followed by a tube. Therefore, knowing the equivalent bending stiffness of the tissue channel after insertion of the needle is essential for predicting the resultant ROC and path planning. Thus, A finite element analysis has been developed for predicting equivalent bending stiffness of the tissue channel after needle insertion.

All SEBS tissue phantoms, Nitinol tubes, and wires involved in finite element analysis are exactly the same as those in experiments. Table II shows the mechanical properties of each tissue phantom, and Table I represents the sizes and mechanical properties of each combination of Nitinol tubes and wires. The complete finite element analysis contains two different parts, both are performed in static structural solver. In the first part, a serial of points are selected along a straight Nitinol stylet, and then the moment reactions on these points are computed based on desired stylet curvature. In the second part, reversed moments are applied on these points along a curved stylet to simulate a pre-loaded straight stylet being released. In the end, resultant radii of curvature are calculated based on displacement results from the FEA. Fig. 4 depicts The FEA modeling to find the resultant ROC of the needle which is a function of bending stiffness of the wire, tube, and soft tissue being inserted.

Manuscript 1655 submitted to 2020 IEEE/RSJ International Conference on Intelligent Robots and Systems. Received March 1, 2020.

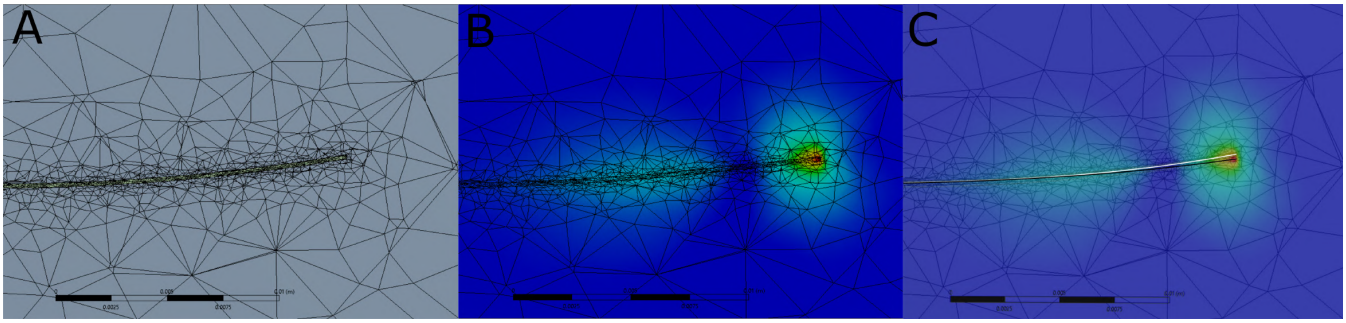

Fig. 4. FEA model of the needle insertion into soft tissue. (A) A straight Nitinol tube is loaded with moments to form the same curvature as the pre-curved tissue channel. (B) Loads are released, and the tissue channel is deformed by Nitinol tube. (C) Overlap of parts A, and B, a clear curvature change can be observed. The centerline of loaded Nitinol tube was marked as white and the centerline of unloaded Nitinol tube was marked as black.

F. Equivalent Bending Stiffness of the Tissue Channel, treat tissue channel as an outer tube

The equations related to the bending stiffness and curvature for calculating multiple overlapped curved tubes has been developed by Webster *et. al.*[9]:

$$\kappa_C = \frac{\sum_{i=1}^{n} E_i I_i \kappa_i}{\sum_{i=1}^{n} E_i I_i} = \frac{K_t \kappa_t + K_b \kappa_b + K_w \kappa_w}{K_t + K_b + K_w} \tag{5}$$

where κ_C is the combined curvature where the tube and wire are fully overlapped, and κ_t, κ_b, κ_w and K_t, K_b, K_w are the curvature and bending stiffness of the tissue channel, tube, and wire, respectively. I_i is the cross-sectional moment of inertia and E is the Young's Modulus.

$$K_i = E_i I_i \tag{6}$$

The product of the Young's Modulus (Modulus of Elasticity) and cross-sectional moment of inertia is bending stiffness. Here is where we make the assumption and treat the tissue channel as an outer tube. Because of the relatively small strains of the tissue using the relative stiffness heuristic, this simplifying assumption is valid.

By switching K_t to the left side, we can obtain equation below from equation(5):

$$K_t = \frac{K_b \kappa_b - K_b \kappa_C + K_w \kappa_w - K_w \kappa_C}{\kappa_C - \kappa_t} \tag{7}$$

Since the Nitinol tubes we used in the experiment are straight and the tissue channel holds the same curvature as the wire, κ_b=0, κ_t=κ_w.

Thus, equation(7) can be written as:

$$K_t = \frac{-K_b \kappa_C + K_w \kappa_w - K_w \kappa_C}{\kappa_C - \kappa_w} \tag{8}$$

G. Experimental Setup

Figure 5-A shows the overall system with the insertion device, overhead camera, a lightbox for transparent tissue simulants, and the associated electronics. Figure 5-B depicts the assembly of the insertion system, with each essential component labeled. Each collet, and bearing was mounted on the opposing linear slides, such that the bores of the collets are collinear. The tube collet is located distally, closest to the insertion point, and the wire collet is located proximally such that the wire can be pushed out of the tube. Three limit switches are located at the most distal limit of travel, the most proximal limit of travel, and between the wire and tube stages.

To develop a predictive model for the tissue channel bending stiffness, the experiments follow the procedures described below:

1) Overlap straight tube and pre-curved wire then fix the ends of them into tube and wire collets, respectively.
2) The wire platform moves forward to insert pre-curved wire into existing channel, which has the same curvature as the wire.
3) Then tube platform follows the wire platform until Nitinol tube and wire are fully overlapped inside the tissue channel.
4) Overhead camera takes photos for curve fitting program written in MATLAB.
5) Retract tube and wire platform and replace tissue, wire and tube with next combination then repeat step 1, 2, 3, and 4.

Since the bending stiffness of the tube in each tube-wire combination is at least one magnitude higher than the bending stiffness of the wire, the tube almost remains straight while they are overlapped. The curvature of the overlapped tube and wire is assumed to be equal to 0.

III. Results

This section describes the compression test results of SEBS tissue phantoms, and the results obtained from multiple sets of experiments with different wire radii, different tube and wire combinations, and different tissue phantoms. Five experiments for each wire radius were conducted, the data presented in figures are the mean value of the experiments.

The approach we used for path tracking is based on image analysis. By fitting curve to the captured image via MATLAB (The MathWorks, Inc., Natick, Massachusetts, United States), the insertion curvature of each tube can be obtained.

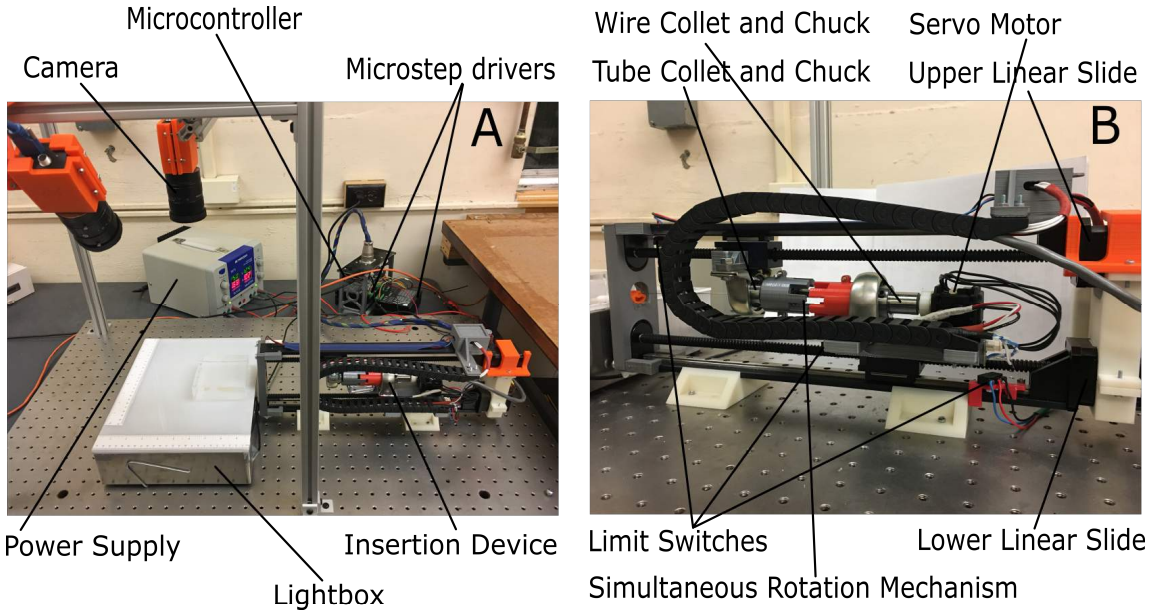

Fig. 5. (A) The whole needle insertion system setup including the insertion device, two micro step drives that drive linear slides, a light box, a camera, a microcontroller, and a power supply. (B) Insertion device setup, including three limit switches, simultaneous rotation mechanism 3D printed by ABS, tube and wire collets and chucks, two linear slides and two bearings.

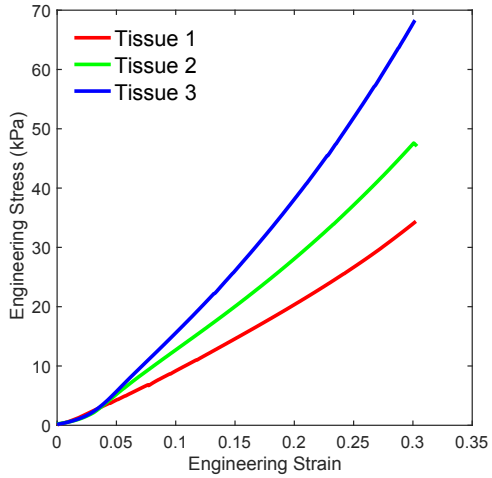

Fig. 6. Stress vs. strain curve of SEBS soft tissue simulants. The Young's modulus of each tissue is obtained by finding the slope of the linear section of the curves. Tissue 1, 2, and 3 are 15%, 20%, and 25% G1650 SEBS in mineral oil soft tissue simulants, respectively.

A. Young's Moduli of SEBS tissues

Figure 6 depicts the stress-strain curve of the soft tissue simulants. The Young's modulus is obtained from finding the slope of the linear section of the curve, and the Young's Moduli of Tissue 1, 2, and 3 are 112.89, 159.80, and 229.57 kPa, respectively. The properties of the soft tissue simulants used in the experiments are provided in Table II.

TABLE II

MECHANICAL PROPERTIES OF SEBS TISSUE PHANTOMS. TISSUES 1, 2, AND 3 ARE 15%, 20%, AND 25% G1650 SEBS IN MINERAL OIL SOFT TISSUE PHANTOMS, RESPECTIVELY.

Tissue Phantom	Density ($\frac{g}{cm^3}$)	Young's Modulus (kPa)	Poisson's ratio
Tissue 1	0.85	112.9	0.49
Tissue 2	0.862	159.8	0.49
Tissue 3	0.865	229.57	0.49

B. Equivalent Bending stiffness of the Tissue Channel, and the Resultant Radius of Curvature

Surface plots of equivalent bending stiffnesses generated from both FEA data and experimental data are provided in Fig. 7. Since equivalent bending stiffness is directly derived from the resultant radius of curvature, these two groups of plots hold high similarity and the equivalent bending stiffness computed from experimental data is marginally higher than FEA in the same type of tissue phantom.

As it is shown in Figure 7, the equivalent bending stiffness of tissue is not only dependent on the bending stiffness of the wire and tube being inserted, but also affected by pre-set channel radius of curvature. In other words, the equivalent bending stiffness of the tissue channel is dependent on the Young's Modulus and cross-sectional moment of inertia of the wire and tube as well as the pre-set wire radius of curvature (during insertion, the tissue channel is always created by the pre-curved wire, so their radii of curvature remain the same). Thus, tissue channel equivalent bending stiffness is a variable that reacts to the inserted stylet, it will increase as the bending stiffness of the stylet increases.

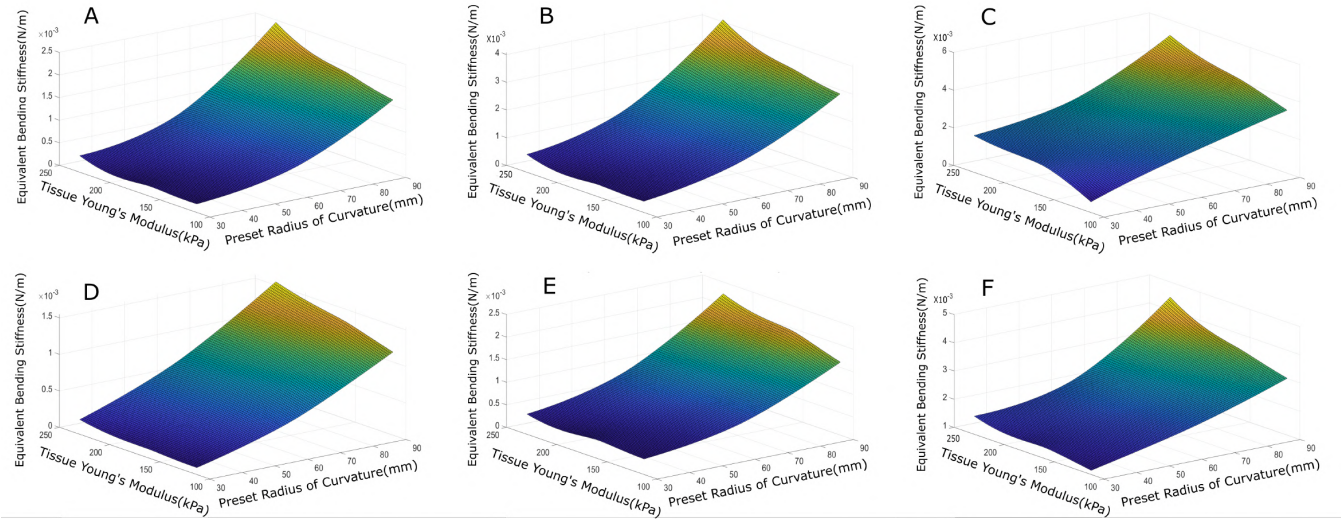

Fig. 7. The equivalent bending stiffness surfaces in experiments and FEA with different tissue phantoms and varying channel radii. (A) The equivalent bending stiffness of tissue channel created by 0.1905mm wire and 0.26mm ID 0.33mm OD tube in experiments. (B) The equivalent bending stiffness of tissue channel created by 0.2921mm wire and 0.3175mm ID 0.5715mm OD tube in experiments. (C) The equivalent bending stiffness of tissue channel created by 0.47mm wire and 0.52mm ID 0.85mm OD tube in experiments. (D) The equivalent bending stiffness of tissue channel created by 0.1905mm wire and 0.26mm ID 0.33mm OD tube in FEA. (B) The equivalent bending stiffness of tissue channel created by 0.2921mm wire and 0.3175mm ID 0.5715mm OD tube in FEA. (C) The equivalent bending stiffness of tissue channel created by 0.47mm wire and 0.52mm ID 0.85mm OD tube in FEA.

The resultant radius of curvature describes the combined radii of curvature of a pre-curved wire, a straight tube and a curved channel in the tissue phantom. The resultant radius of curvature depends on the bending stiffnesses of the wire, tube and tissue channel. Three dimensional surfaces were fit on both FEA data and experimental data.

In experiments, the insertion of 0.85mm diameter tube exceeded the tolerance of the tissue channel in Tissue 1 for 30mm radius channel. It couldn't follow the inner wire properly and tend to break through the boundary of the channel after the first 10-12mm during insertion because of the tight curvature of the channel and its high bending stiffness. The FEA provided a reasonable prediction for 30mm channel in Tissue 1 when high bending stiffness tube being inserted, the reason is that the tube were pre-loaded and pre-bend then put into the channel, so the pressure exerted on the channel wall was smooth and uniform. In reality, it's arduous to duplicate the setup we used in FEA, so we used a different approach to obtain the resultant radius of curvature. Since the FEA and experimental data have high similarity, the FEA data will be used to replace this specific data point when discussing tissue behavior in future sections.

By comparing the FEA data with experimental data, it's obvious that the resultant radius of curvature in experiments are slightly lower than the resultant radius of curvature in FEA except for the data point where the high bending stiffness tube inserted in Tissue 1 at 30mm channel. A hypothesis is that some of the mineral oil was escaped from the phantoms during storage since the experiments were conducted in around two days. The ratio rise of SEBS polymer will result in a stiffer tissue phantom which caused a decrease in resultant curvature.

In general, if tube and wire are selected, the stiffer the tissue phantom is, the smaller the resultant radius of curvature is. On the other hand, if tissue phantom has a specific Young's Modulus, the larger the bending stiffness of the tube, the larger the resultant radius of curvature is.

IV. Discussion

In this paper, series of experiments are conducted to derive the resultant radius of curvature from the bending stiffness of the tube and wire, the pre-set curvature of the tissue channel and the Young's Modulus of the tissue. A finite element analysis is also developed to provide support for the reliability of the resultant radius model. To achieve a quality insertion with scarce tissue damage, the bending stiffness of the wire should be approximately one magnitude lower than the bending stiffness of the tube. If the bending stiffness of the wire is too close to the bending stiffness of the tube, the combined curvature of the tube and wire will be relatively high which increases the difficulty at the beginning of the insertion. If the bending stiffness of the wire is too low from the bending stiffness of the tube, it's harder for the tube to follow the wire in relatively soft tissue. Since the equivalent bending stiffness of tissue channel is a variable that reacts to the inserted stylet in this model, further research which also takes step length into consideration is needed to provide a complete model of resultant insertion radius of curvature. The similarity of the models obtained from both FEA and experiments reveals that the insertion radius of curvature is predictable by given the mechanical properties of the combination of tissue phantom, tube, and wire at a selected step length.

V. Conclusion and Future Work

We have presented a method of treating tissue channel as an outer tube and an approach to predict the resultant radius of

Manuscript 1655 submitted to 2020 IEEE/RSJ International Conference on Intelligent Robots and Systems. Received March 1, 2020.

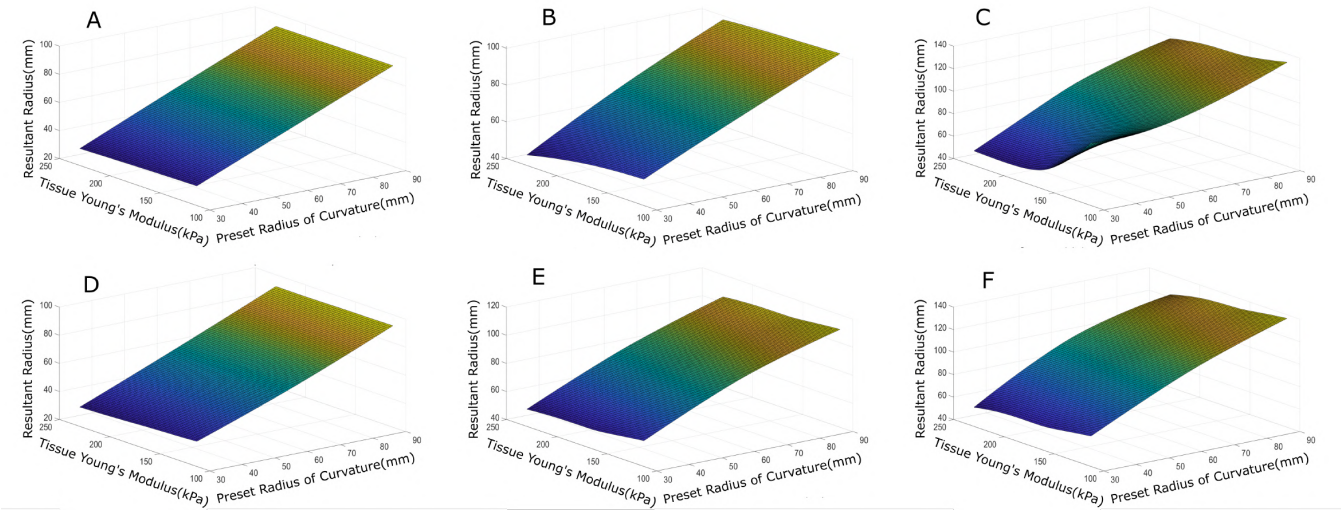

Fig. 8. Resultant radii of curvature surfaces in experiments and FEA with different tissue phantoms and varying channel radii. (A) 0.33mm OD, 0.26mm ID tube, and 0.19mm wire in experiments. (B) 0.57mm OD, 0.32mm ID tube, and 0.29mm wire in experiments. (C) 0.85mm OD, 0.52mm ID tube, and 0.47mm wire in experiments. (D) 0.33mm OD, 0.26mm ID tube, and 0.19mm wire in FEA. (E) 0.57mm OD, 0.32mm ID tube, and 0.29mm wire in FEA. (F) 0.85mm OD, 0.52mm ID tube and 0.47mm wire in FEA.

curvature for fracture-directed stylet-and-tube needle steering technique. The experiments conducted for the resultant radius of curvature serve as a part of fracture directed steerable needle research. The model can be expanded across a wider range of tissues' Young's Moduli or pre-set wire curvatures by simply conducting experiments on the target data field. By combining with the step length model, a complete model for a specific insertion can be described as

$$\kappa_r = \mathrm{f}(\ell,\ K_w,\ K_b,\ K_t,\ \kappa_w,\ \kappa_b)$$

where κ_r is the insertion curvature, ℓ is step length, κ_t, κ_b, κ_w and K_t, K_b, K_w are the curvature and bending stiffness of the tissue channel, tube, and wire, respectively.

The prompt future work is to accomplish the establishment of the complete predictive model and develop a path planning algorithm for vision-based closed-loop control. This vision-based closed-loop control system will provide the capability of control to any planned path within achievable insertion radius. Fracture directed steerable needles furnished a new class of needles for future research which can be potentially used for multiple industrial and medical purposes.

REFERENCES

[1] F. Yang, M. Babaiasl, and J. P. Swensen, "Fracture-directed steerable needles," *Journal of Medical Robotics Research*, p. 1842002, 2018.

[2] T. K. Adebar, J. D. Greer, P. F. Laeseke, G. L. Hwang, and A. M. Okamura, "Methods for improving the curvature of steerable needles in biological tissue," *IEEE Transactions on Biomedical Engineering*, vol. 63, no. 6, pp. 1167–1177, 2015.

[3] G. Lapouge, J. Troccaz, and P. Poignet, "Multi-rate unscented kalman filtering for pose and curvature estimation in 3d ultrasound-guided needle steering," *Control Engineering Practice*, vol. 80, pp. 116–124, 2018.

[4] S. Misra, K. B. Reed, A. S. Douglas, K. Ramesh, and A. M. Okamura, "Needle-tissue interaction forces for bevel-tip steerable needles," in *Biomedical Robotics and Biomechatronics, 2008. BioRob 2008. 2nd IEEE RAS & EMBS International Conference on*. IEEE, 2008, pp. 224–231.

[5] S. Misra, K. Ramesh, and A. M. Okamura, "Modeling of tool-tissue interactions for computer-based surgical simulation: a literature review," *Presence: Teleoperators and Virtual Environments*, vol. 17, no. 5, pp. 463–491, 2008.

[6] T. Watts, R. Secoli, and F. R. y Baena, "A mechanics-based model for 3-d steering of programmable bevel-tip needles," *IEEE Transactions on Robotics*, vol. 35, no. 2, pp. 371–386, 2018.

[7] D. C. Rucker, R. J. Webster III, G. S. Chirikjian, and N. J. Cowan, "Equilibrium conformations of concentric-tube continuum robots," *The International journal of robotics research*, vol. 29, no. 10, pp. 1263–1280, 2010.

[8] B. C. W. Kot, Z. J. Zhang, A. W. C. Lee, V. Y. F. Leung, and S. N. Fu, "Elastic modulus of muscle and tendon with shear wave ultrasound elastography: variations with different technical settings," *PloS one*, vol. 7, no. 8, p. e44348, 2012.

[9] R. J. Webster III, J. M. Romano, and N. J. Cowan, "Mechanics of precurved-tube continuum robots," *IEEE Transactions on Robotics*, vol. 25, no. 1, pp. 67–78, 2009.

[10] R. A. Mrozek, B. Leighliter, C. S. Gold, I. R. Beringer, H. Y. Jian, M. R. VanLandingham, P. Moy, M. H. Foster, and J. L. Lenhart, "The relationship between mechanical properties and ballistic penetration depth in a viscoelastic gel," *Journal of the mechanical behavior of biomedical materials*, vol. 44, pp. 109–120, 2015.

[11] M. Babaiasl, F. Yang, Y. Chen, J.-L. Ding, and J. P. Swensen, "Predicting depth of cut of water-jet in soft tissue simulants based on finite element analysis with the application to fracture-directed water-jet steerable needles," in *2019 International Symposium on Medical Robotics (ISMR)*. IEEE, 2019, pp. 1–7.

[12] M. Babaiasl, F. Yang, and J. P. Swensen, "Towards water-jet steerable needles," in *2018 7th IEEE International Conference on Biomedical Robotics and Biomechatronics (Biorob)*. IEEE, 2018, pp. 601–608.

[13] Z. Khashei Varnamkhasti and B. Konh, "Design and performance study of a novel minimally invasive active surgical needle," *Journal of Medical Devices*, vol. 13, no. 4, 2019.

[14] M. J. Oldfield, A. Leibinger, T. E. T. Seah, and F. R. y Baena, "Method to reduce target motion through needle–tissue interactions," *Annals of biomedical engineering*, vol. 43, no. 11, pp. 2794–2803, 2015.

[15] M. G. Jushiddi, J. J. Mulvihill, D. Chovan, A. Mani, C. Shanahan, C. Silien, S. A. M. Tofail, and P. Tiernan, "Simulation of biopsy bevel-tipped needle insertion into soft-gel," *Computers in biology and medicine*, vol. 111, p. 103337, 2019.